Observations and calculations of light scattering from clusters of spheres

Stephen Holler, Jean-Claude Auger, Brian Stout, Yongle Pan, Jerold R. Bottiger, Richard K. Chang, and Gorden Videen

Two-dimensional angular optical scattering (TAOS) patterns from clusters of polystyrene latex spheres are measured in the near-forward and near-backward directions. In both cases, the scattering pattern contains a rich and complicated structure that is the result of the interaction and interference of light among the primary particles. Calculations are made for aggregates that are similar to those generated experimentally and also demonstrate the rich structure in the scattering pattern. A comparison of the experimental and theoretical TAOS patterns gives good qualitative agreement. © 2000 Optical Society of America

OCIS codes: 290.5820, 290.4020, 290.5850, 290.4210, 010.1110.

1. Introduction

Recently there has been experimental[1–3] and theoretical[2,4–7] interest in the optical properties of airborne microparticle aggregates. Such aerosols have been found to play important roles in a myriad of fields including industrial, environmental, and health sciences,[8] atmospheric remote sensing,[9] and astrophysical studies of scattering by planetary[10] and interstellar[11] dust particles. This is so primarily because many interesting or potentially harmful (or both) materials form clusters of smaller primary particles. For example, carbon (soot) particles, which play an important role in the heat balance of the Earth, are often found in fractal aggregates.[12] Despite the fact that the primary particles may be in the Rayleigh regime, the overall cluster is not, and it exhibits fundamentally different optical properties. Other sys-tems of interest include dense clusters of spores, which can pose a threat as biological warfare agents.[13] One possible means for determining shape and structure information about airborne microparticles is to investigate their angular light scattering. Often this is done in only one angular dimension (θ). However, a growing number of researchers are presenting the angular intensity distribution of the scattered light as a function of two angles (θ, ϕ).[3,7,14–17] Because the elastic scattered angular intensity distribution from nonspherical particles (e.g., microparticle aggregates, oblate and prolate spheroids) has an azimuthal (ϕ) as well as a polar (θ) dependence, observation of two-dimensional angular optical scattering (TAOS) is useful for determining shape and structure information about such nonspherical particles.

In what follows, we present a comparison between theory and experiment of the TAOS from a three-dimensional close-packed cluster of spherical primary particles. In Section 2 we discuss the theoretical technique for calculating light scattering from an aggregate. In Section 3 we highlight the experimental arrangement and discuss the generation of the clusters. We present the experimental and theoretical results in Section 4. In Section 5 we summarize our study and present ideas for future investigations. Finally, in Appendix A we outline the translation addition theorem for spherical wave functions and discuss some relevant aspects for the computational work.

2. Theory

In this section we develop a model that can be used to calculate the differential scattering cross section of

an aggregate composed of many dielectric spheres. Mie introduced in 1908 the exact solution for the scattering of a plane electromagnetic wave by a single isotropic homogeneous sphere.[18] The vector wave equation can be derived by use of various devices and approaches, such as Hertz vectors,[19] separation of variable solutions (by means of the scalar-wave equation),[20] and the T-matrix formalism introduced by Waterman.[21] We have chosen the last-named approach because it can be extended to derive the theoretical solution of the multiple scattering of light by an aggregate of spheres. The model includes the multiple scattering that occurs among the spheres, and the formulation is developed to optimize calculations.

A. Vector Wave Equation

In a spherical coordinate system, the linear independent solutions of the vector wave equation (Helmholtz equation) in a source-free homogeneous medium are the independent, divergenceless vector spherical wave functions $\Psi_{\sigma mn}(kr, \theta, \phi)$:

$$\Re e\ \Psi_{1mn}(kr, \theta, \phi) = \sqrt{\gamma mn} \left\{ \left[\frac{im}{\sin\theta} j_n(kr) \right] P_n^m(\cos\theta) \right.$$

$$\times \exp(im\phi)\hat{\theta} - j_n(kr)\frac{\partial}{\partial\theta} P_n^m$$

$$\left. \times (\cos\theta)\exp(im\phi)\hat{\phi} \right\}, \qquad (2.1)$$

$$\Re e\ \Psi_{2mn}(kr, \theta, \phi) = \sqrt{\gamma mn} \left\{ \frac{n(n+1)}{kr} j_n(kr) P_n^m(\cos\theta) \right.$$

$$\times \exp(im\phi)\hat{r} + \left[\frac{1}{kr}\frac{\partial}{\partial r} rj_n(kr) \right] \frac{\partial}{\partial\theta} P_n^m(\cos\theta)$$

$$\times \exp(im\phi)\hat{\theta} + \left[\frac{im}{kr\sin\theta}\frac{\partial}{\partial r} rj_n(kr) \right] P_n^m(\cos\theta)$$

$$\left. \times \exp(im\phi)\hat{\phi} \right\}, \qquad (2.2)$$

where $j_n(kr)$ are spherical Bessel functions of the first kind that have the complex argument kr, $k = 2\pi/\lambda$ is the propagation constant for the medium, and $P_n^m(\cos\theta)$ are the associated Legendre functions of the first kind and of degree n and order m, where n and m are integers defined in the intervals $1 \leq n \leq \infty$ and $-n \leq m \leq n$. The time-harmonic convention is $\exp(-i\omega t)$. The factor

$$\gamma_{mn} = \frac{(2n+1)(n-m)!}{4\pi n(n+1)(n+m)!}$$

serves to normalize the spherical wave functions with the angular variables θ and ϕ. At large r, the scattered fields can be expressed by the vectors $\Psi_{imn}(kr, \theta, \phi)$ that we obtained by replacing the Bessel functions $j_n(kr)$ with the Hankel functions of the first kind $h_n^{(1)}(kr) = j_n(kr) + iy_n(kr)$; then $\Re e$ stands for the regular part of.

Consider a medium of real refractive index n_0 for which a plane electromagnetic wave characterized by propagation constant k_0 and wavelength λ_0 impinges upon a dielectric sphere of complex refractive index n_1 and propagation constant k_1. According to Mie theory, the incident field ($\mathbf{E}_{inc}$, $\mathbf{H}_{inc}$) and the scattered field ($\mathbf{E}_{sca}$, $\mathbf{H}_{sca}$) can be expanded in terms of an infinite series of spherical vector wave functions:

$$\mathbf{E}_{inc} = \sum_{n=1}^{n=\infty} \sum_{m=-n}^{m=n} (a_{1mn} \Re e\ \Psi_{1mn} + a_{2mn} \Re e\ \Psi_{2mn})$$

$$= \sum_{\sigma,m,n} a_{\sigma mn} \Re e\ \Psi_{\sigma mn},$$

$$\mathbf{H}_{inc} = \frac{1}{i\eta_0} \sum_{n=1}^{n=\infty} \sum_{m=-n}^{m=n} (a_{2mn} \Re e\ \Psi_{1mn} + a_{1mn} \Re e\Psi_{2mn}); \qquad (2.3)$$

$$\mathbf{E}_{sca} = \sum_{n=1}^{n=\infty} \sum_{m=-n}^{m=n} (f_{1mn} \Psi_{1mn} + f_{2mn} \Psi_{2mn})$$

$$= \sum_{\sigma,m,n} f_{\sigma mn} \Re e\ \Psi_{\sigma mn},$$

$$\mathbf{H}_{sca} = \frac{1}{i\eta_0} \sum_{n=1}^{n=\infty} \sum_{m=-n}^{m=n} (f_{2mn} \Psi_{1mn} + f_{1mn} \Psi_{2mn}), \qquad (2.4)$$

where $\eta_0 = \omega\mu/k_0$.

B. T Matrix for a Single Dielectric Sphere

The T matrix introduced by Waterman[21] ($\bar{\mathbf{T}}$) converts the expansion coefficients of the incident wave ($a_{\sigma mn}$) impinging upon an arbitrarily shaped particle into the expansion coefficients of the radiated scattering wave ($f_{\sigma mn}$) through the relation

$$\mathbf{f} = \bar{\mathbf{T}}\mathbf{a}. \qquad (2.5)$$

The elements of the T matrix are independent of the incident and scattered fields. They depend only on the intrinsic features of the scattering particle (shape, size parameter, and complex refractive index) and on its orientation with respect to the coordinate system. For a spherical particle, the elements of the T matrix are greatly simplified, and it is now well known that applying the boundary condition on the spherical interface yields

$$T_{1mn,1m'n'} = -\delta_{mm'}\delta_{nn'}$$

$$\times \frac{j_n(k_1 r_0)[k_0 r_0 j_n(k_0 r_0)]' - j_n(k_0 r_0)[k_1 r_0 j_n(k_1 r_0)]'}{j_n(k_1 r_0)[k_0 r_0 h_n(k_0 r_0)]' - h_n(k_0 r_0)[k_1 r_0 j_n(k_1 r_0)]'}, \qquad (2.6)$$

$$T_{2mn,2m'n'} = -\delta_{mm'}\delta_{nn'}$$

$$\times \frac{(k_1^2/k_0^2)j_n(k_1 r_0)[k_0 r_0 j_n(k_0 r_0)]' - j_n(k_0 r_0)[k_1 r_0 j_n(k_1 r_0)]'}{(k_1^2/k_0^2)j_n(k_1 r_0)[k_0 r_0 h_n(k_0 r_0)]' - h_n(k_0 r_0)[k_1 r_0 j_n(k_1 r_0)]'}, \qquad (2.7)$$

$$T_{1mn,2m'n'} = T_{2mn,1m'n'} = 0, \qquad (2.8)$$

where the primes denote derivatives with respect to the arguments of the Bessel functions.

C. Expansion of the Incident Plane Wave

The incident plane wave can be expanded in terms of vector spherical wave functions for both polarization states, transverse electric and transverse magnetic (TE and TM), respectively:

$$a_{1mn}^{\text{TM}} = \sqrt{\zeta_{mn}}\, i^{n+3}\, \frac{m}{\sin\theta_i}\, P_n^m(\cos\theta_i)\exp(-im\phi_i), \quad (2.9)$$

$$a_{2mn}^{\text{TM}} = \sqrt{\zeta_{mn}}\, i^{n+3}\, \frac{\mathrm{d}}{\mathrm{d}\theta}\, P_n^m(\cos\theta_i)\exp(-im\phi_i), \quad (2.10)$$

$$a_{1mn}^{\text{TE}} = \sqrt{\zeta_{mn}}\, i^{n+2}\, \frac{\mathrm{d}}{\mathrm{d}\theta}\, P_n^m(\cos\theta_i)\exp(-im\phi_i), \quad (2.11)$$

$$a_{2mn}^{\text{TE}} = \sqrt{\zeta_{mn}}\, i^{n+2}\, \frac{m}{\sin\theta_i}\, P_n^m(\cos\theta_i)\exp(-im\phi_i), \quad (2.12)$$

where the factor

$$\zeta_{mn} = \frac{4\pi(2n+1)(n-m)!}{n(n+1)(n+m)!}$$

is introduced for consistency with the normalization chosen for Eqs. (2.1) and (2.2).

D. Basis of the Analytical Problem

Consider a cluster of N isotropic, homogeneous, compact, randomly dispersed spheres with radii a_i and complex refractive indices n_s^i. The center of each sphere O_i is defined in a principal coordinate system $\mathbf{R}_0$ by a position vector $\mathbf{r}_i$. The relative position vector between two arbitrary spheres i and j is defined by $\mathbf{r}_{ij}$. On application of the superposition principle of electromagnetic theory, the total external field $\mathbf{E}_{\text{tot}}$ is the summation of the incident wave from the original source $\mathbf{E}_{\text{inc}}$ with all the scattered fields $\mathbf{E}_{\text{sca}}^i$:

$$\mathbf{E}_{\text{tot}} = \Re e\, \Psi(k_0|\mathbf{r}-\mathbf{r}_0|)\mathbf{a}^0 + \sum_{i=1}^{N} \Psi(k_0|\mathbf{r}-\mathbf{r}_i|)\mathbf{f}^{i(N)}. \quad (2.13)$$

Solving the total electric field scattered by an aggregate of spheres amounts to evaluating the scattered field from each individual sphere in the cluster. It is then necessary to translate the entire scattered field on a common basis to get an exact single analytical expression of the total field scattered by the aggregate.

E. Solving the Multiple-Scattering Equation

In multiple-scattering theory, the field incident upon the ith scatterer is due to the contribution of the field from the original source $\mathbf{E}_{\text{inc}}$ and the scattered fields $\mathbf{E}_{\text{sca}}^i$ from the other j particles in the cluster. This field, called the excitation field, $\mathbf{E}_{\text{exc}}^i$, has the formulation

$$\mathbf{E}_{\text{exc}}^i = \mathbf{E}_0 + \sum_{\substack{j=1\\j\neq 1}}^{N} \mathbf{E}_{\text{sca}}^j. \quad (2.14)$$

The T-matrix formulation [Eq. 2.5] leads to the relation $\mathbf{E}_{\text{sca}}^i = \bar{\mathbf{T}}^{i(1)}\mathbf{E}_{\text{exc}}^i$, where $\bar{\mathbf{T}}^{i(1)}$ is the isolated-scatterer T matrix for the ith scatterer. Then, using the expansion in terms of spherical vector wave functions of each field, we have

$$\mathbf{E}_{\text{sca}}^i = \bar{\mathbf{T}}^{i(1)}\left[\Re e\, \Psi(k_0|r-r_0|)\mathbf{a}^0 + \sum_{\substack{j=1\\j\neq i}}^{N} \Psi(k_0|r-r_i|) f^{j(N)} \right]. \quad (2.15)$$

In Eq. (2.15), the incident field is expanded in the principal coordinate system $R_0(kr_0,\theta_0,\phi_0)$, whereas the scattered fields from each sphere are expressed in the coordinate systems of the scatterers $R_j(kr_j,\theta_j,\phi_j)$. To solve the multiple-scattering problems it is necessary to express both terms in the ith-scatterer coordinate system. When the translational addition theorem for the spherical vector wave functions [Eqs. (A1) and (A2) below] is applied and the expansion coefficient representation of each field [Eq. (2.15)] is used,

$$f^{j(N)} = \bar{\mathbf{T}}^{i(1)}\left[\bar{\beta}(i,0)\mathbf{a}^0 + \sum_{\substack{j=1\\j\neq i}}^{N} \bar{\alpha}(i,j) f^{j(N)} \right],$$
$$i = 1,\ldots,N, \quad (2.16)$$

where $\bar{\beta}(i,0)$ and $\bar{\alpha}(i,j)$ are the translation matrices for the incident and the scattered fields, respectively. Equation (2.16) defines a group of N-coupled linear equations whose unknown variables are the expansion coefficients of the scattered field of each individual sphere. The solution can be found by use of various techniques such as the order of scattering,[4] the direct inversion matrix, and the iteration method.[22,23] Nevertheless, it is convenient to introduce $\bar{\mathbf{T}}^{i(N)}$, the N-scatterer T matrix of the ith scatterer. This formulation includes all the information about multiple-scattering effects caused by the presence of N scatterers, which directly links incident field E_0 to the scattered field of the ith scatterer by the equation

$$\mathbf{f}^{i(N)} = \bar{\mathbf{T}}^{i(N)}\mathbf{a}^i = \bar{\mathbf{T}}^{i(N)}\bar{\beta}(i,0)\mathbf{a}^0. \quad (2.17)$$

As $\mathbf{f}^{i(N)}$ is defined in the coordinate system of the ith scatterer, $\mathbf{a}^i$ is also. Then, from Eq. (2.13) and by application of the translational addition theorem [Eq. (A3) below] once more, the total scattered field coefficients in the principal coordinate system have the form

$$\mathbf{f}^{T(N)} = \sum_{i=1}^{N} \bar{\beta}(0,i)\bar{\mathbf{T}}^{i(N)}\bar{\beta}(i,0)\mathbf{a}^0. \quad (2.18)$$
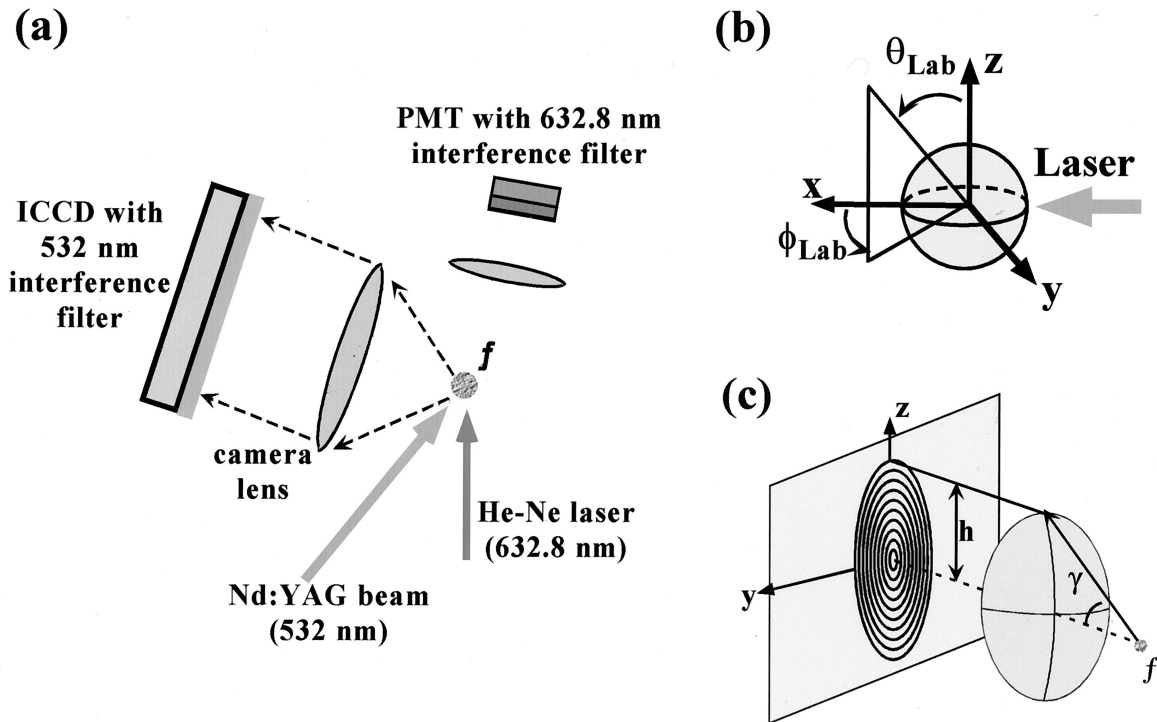
Fig. 1. (a) Experimental setup used for the TAOS measurements, (b) the laboratory-coordinate system, (c) an illustration of the Abbé sine condition.

It is possible to introduce the global T matrix of the cluster $\bar{T}^{T(N)}$ that directly converts the incident field coefficients into the total scattered field coefficients:

$$\mathbf{f}^{T(N)} = \bar{\mathbf{T}}^{T(N)}\mathbf{a}^0, \tag{2.19}$$

with

$$\bar{\mathbf{T}}^{T(N)} = \sum_{i=1}^{N} \bar{\beta}(0, i)\bar{\mathbf{T}}^{i(N)}\bar{\beta}(i, 0). \tag{2.20}$$

The global T matrix is independent of the incident field and depends only on cluster configuration; therefore it can be used in computations for any direction and polarization state of the incident wave. It is also useful for computing orientationally averaged light scattering through use of the rotational addition theorem.

Substituting Eq. (2.17) into Eq. (2.16) results in a new linear matrix equation in which the unknown variables are the N-scatterer T matrices of each sphere. This system can be solved by use of an iterative or a recursive algorithm.[5,24] However, for certain cases of dense aggregates the iterative algorithm cannot converge because the method assumes that the primary contribution to it is the incident field. For this reason we use the recursive T-matrix algorithm (RTMA) developed by Chew[24] as the basis

of our study. The results can be expressed by these two equations[24]:

$$\bar{\mathbf{T}}^{N+1(N+1)}\bar{\beta}(N + 1, 0) = \left[\bar{\mathbf{I}} - \bar{\mathbf{T}}^{N+1(1)} \sum_{i=1}^{n} \bar{\alpha}(N + 1, i)\right.$$
$$\left. \times \bar{\mathbf{T}}^{i(N)}\bar{\beta}(i, 0)\bar{\alpha}(0, N + 1)\right]^{-1}$$
$$\times \bar{\mathbf{T}}^{N+1(1)}\left[\bar{\beta}(N + 1, 0) + \sum_{i=1}^{n} \bar{\alpha}(N\right.$$
$$\left. + 1, i)\bar{\mathbf{T}}^{i(N)}\bar{\beta}(i, 0)\right], \tag{2.21}$$

$$\bar{\mathbf{T}}^{i(N+1)}\bar{\beta}(i, 0) = \bar{\mathbf{T}}^{i(N)}\bar{\beta}(i, 0)[\bar{\mathbf{I}} + \bar{\alpha}(0, \mathbf{N} + 1)$$
$$\times \bar{\mathbf{T}}^{N+1(N+1)}\bar{\beta}(N + 1, 0)], \quad i \leq N. \tag{2.22}$$

The $(N + 1)$ sphere in the aggregate acts as a perturbation for the whole system. Then the individual multiple-scattering T matrices $\bar{\mathbf{T}}^{i(N+1)}$ of the $(N + 1)$ sphere cluster are evaluated from the individual multiple-scattering T matrices $\bar{\mathbf{T}}^{i(N)}$ of the N-sphere cluster.

3. Experiment

The experimental setup is shown in Fig. 1(a). It consists of a particle generator to create the clusters and an apparatus to illuminate the clusters and measure their two-dimensional angular scattering pattern. Clusters of polystyrene latex (psl) spheres are generated with an ink-jet aerosol generator[25] (IJAG)

from a solution of psl spheres and water loaded into an empty ink-jet cartridge (Hewlett-Packard, 51612A BlankJet), which is mounted upon the IJAG's drying column. The IJAG controller box sequentially triggers (either from 1 to 2 kHz or singly on demand) each of the 12 nozzles in the cartridge to produce water droplets (50-μm diameter) that contain psl sphere inclusions. The number of primary particles within a water droplet follows Poisson statistics and depends on the concentration of slurry within the cartridge. By varying the concentration, one may generate clusters of different sizes. After being ejected from the ink-jet cartridge, the droplets are often accompanied by small satellite droplets. These secondary droplets are removed with a winnow flow while the large primary droplet is entrained within an airflow that carries it through the drying column. The drying column is heated to ~105 °C so that, as the wet droplets with inclusions traverse the column, the water evaporates, leaving a dry aggregate of primary particles. At the end of the column is a tapered nozzle with a 1-mm exit port. The clusters emerge from the nozzle and fall into the scattering volume of the measuring apparatus.

Although the IJAG may fire periodically, the changing droplet size and the irregular shape of the aggregates prevent the clusters from emerging in a periodic fashion. Because of the asynchronous passage of particles through the scattering volume, it is necessary to detect when a cluster is in the correct location. The presence of a falling cluster is detected with a cw He–Ne trigger laser (632.8 nm) and a photomultiplier tube (PMT) with a narrow-bandpass filter. As the aggregate enters the scattering volume, it crosses the He–Ne trigger beam and scatters light toward the PMT. Detection of a signal with the PMT initiates the trigger sequence for the TAOS measurement.

On receiving a trigger pulse, the second harmonic (λ = 532 nm) of a Q-switched (30-ns pulse) Nd:YAG laser illuminates the falling cluster. The elastic scattered light is then collected in either the near-forward or the near-backward region with an $f/\# = 1.2$ camera lens used in the Abbé sine condition[26]: In this condition, the lens is positioned such that the falling particle is in the back focal plane of the lens. A ray of light that scatters off the particle and enters the lens at an angle γ emerges parallel, with a displacement h given by

$$h = f \sin \gamma, \qquad (3.1)$$

where f is the focal length of the lens. The emerging parallel light is then recorded with an intensified CCD (ICCD) camera with a narrow-bandpass filter such that only the scattered 532-nm light is recorded.

For our experiments, the coordinate system of the laboratory is taken such that the clusters fall in the $-z$ direction and the laser propagates parallel to the x axis [Fig. 1(b)]. The Abbé sine condition then relates the y–z coordinate of the ICCD camera to the θ_{lab}–ϕ_{lab} scattering angles in the laboratory frame. The geometry of the sine condition is shown in Fig.

1(c). This choice of coordinate system is nonstandard when TAOS calculations are performed. Typically, and as is done for our calculations, the laser propagates along the z axis. In this case, the aggregates would be falling in the $-x$ direction. The correspondence between the calculation and the laboratory frames is such that $(x, y, z)_{calc} \leftrightarrow (z, -y, x)_{lab}$. To make comparisons between experimental results and theoretical calculations, it is useful to transform the calculations into the laboratory-frame coordinate system. We do so by comparing the two coordinate systems and utilizing the sine condition of Eq. (3.1). The resultant transformation is

$$\theta_{lab} = \cos^{-1}(\sin \theta_{calc} \cos \phi_{calc}),$$
$$\phi_{lab} = \phi_0 + (-1)^j \sin^{-1}(-\sin \theta_{calc} \sin \phi_{calc}), \quad (3.2)$$

where θ_{lab} and ϕ_{lab} are the scattering angles in the laboratory coordinate frame, θ_{calc} and ϕ_{calc} are the scattering angles in the calculation frame, and ϕ_0 is either 0° with $j = 0$ for forward scattering or 180° with $j = 1$ for backward scattering.

4. Results and Discussion

To ensure the proper operation of our apparatus, we performed TAOS measurements on single psl spheres of two different sizes. Dilute solutions of 22-μm- and 2.29-μm-diameter psl spheres were prepared and loaded into ink-jet cartridges. The observed TAOS patterns for both sizes were consistent with Mie theory, demonstrating the ring structure associated with light scattering from a sphere. With this verification, we could confidently perform TAOS measurements on aggregates of the 2.29-μm-diameter psl spheres.

Aggregates of 2.29-μm-diameter psl spheres (refractive index $n = 1.59$) are created with the IJAG. The slurry is mixed at 0.7 mg of spheres/ml of water. In addition, a small amount (0.01%) of surfactant (Tween-20) is added to the water to improve the mixture's flow properties (necessary for passage inside the narrow channels of the cartridge). The clusters are characterized with an aerodynamic particle sizer, scanning-electron microscopy, and optical microscopy. We determined the average number of spheres per cluster by turning off the oven heater and allowing it to cool. Wet droplets containing psl spheres are allowed to fall through the column and splatter onto a microscope slide. The water in each splat evaporates, leaving a monolayer of particles that we count with an optical microscope to determine the average number of primary particles per cluster.

We can infer the uniformity of the droplets by counting the number of primary particles included in a sampling of droplets. In Fig. 2 we show the results of counting the number (N_{sph}) of 2.29-μm psl spheres in each of 227 randomly selected splats of wet droplets. The fraction of the 227 clusters that contains N_{sph} spheres is plotted versus N_{sph}. The most probable number of spheres was found to be 18. Also plotted is the Poisson distribution probability of finding N_{sph} spheres in a cluster, given that the average
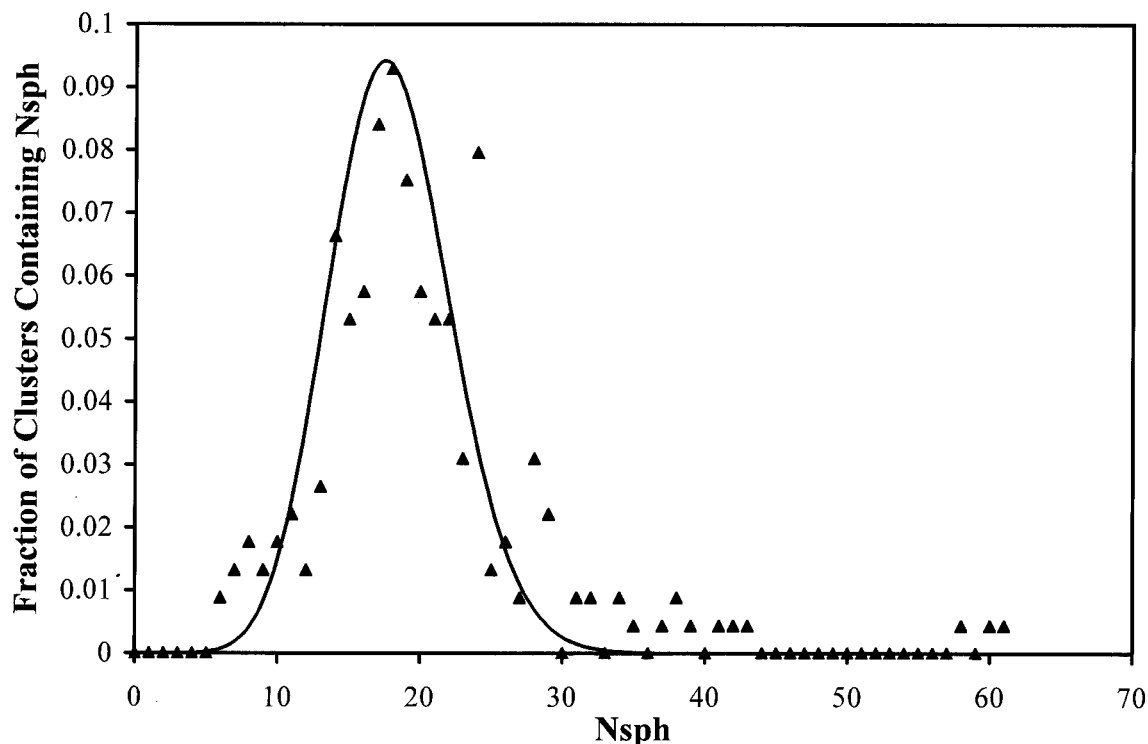
Fig. 2. Fraction of the 227 clusters that contain N_{sph} spheres plotted versus N_{sph}. The solid curve represents a Poisson distribution, given that the most probable number of spheres is 18.

N_{sph} is 18. The two sets of data are in good agreement, as one would expect if the original droplets were monodisperse. The data points that indicate more than ~40 spheres in a cluster are probably where two or three droplets hit the microscope slide at the same location. Geometric sizing with a scanning-electron microscope (SEM) showed that this cluster sample has a mean geometric diameter of 6.7 μm. Figure 3(a) shows a SEM micrograph of a typical psl cluster.

Calculations are performed for a close-packed cluster containing primary particles that have the same size parameter ($x_{p.p.} = 2\pi a/\lambda \approx 13.3$) as those used in the experiment. To make the aggregate size parameter comparable with the mean experimental size parameter ($x_{clus.} \approx 40$), we arrange 13 spheres as shown in Fig. 3(b). The coordinates of each of the primary particles are given in Table 1. Because falling clusters in the experiment are randomly oriented, the calculations were performed at different tilt angles (τ) so a reasonable comparison could be made. Figure 3(b) shows the Mathematica default view of the theoretically generated cluster. The view along the calculation z axis, i.e., the view of the cluster seen from the illuminating laser, for the untilted cluster (τ = 0°) is shown in Fig. 3(c). Tilting the cluster through τ = 5° yields a slightly different view from that seen in Fig. 3(c) (not shown). The cluster tilted by τ = 45° and viewed from the illuminating laser is shown in Fig. 3(d). The cluster seen in this orientation is remarkably similar to that shown in the SEM micrograph of Fig. 3(a).

The random orientation of the aggregates emerging from the IJAG makes it impossible to know for which angles to calculate the TAOS. Because of this uncertainty, we chose to look at three orientations (τ = 0°, 5°, 45°). To get a sense of what the numerical calculations of the TAOS look like in the laboratory-coordinate frame, we used Eqs. (3.2) to transform the calculations. The resultant transformed forward and backward TAOS calculations for the three orientations considered are shown in Fig. 4. Because of the high-intensity forward-scattering peak, the forward-scattering calculations are plotted on a log scale. Also shown are the regions observed experimentally. In the forward direction, the TAOS measurements are made for $16° \leq \theta_{calc} \leq 44°$, whereas the near-backward observations are made for $120° \leq \theta_{calc} \leq 148°$. These angular regions correspond to the areas bounded by the white circles. The actual angular coverage of the detector is denoted in each case by a small white-bordered rectangle.

Our comparisons are limited to three tilt angles that allow us to view the cluster in three representative orientations: one of high symmetry, one with slightly less symmetry, and one whose symmetry has been broken. However, the falling aggregates are also free to rotate in the ϕ_{calc} direction. Rather than calculating at a number of different (θ_{calc}, ϕ_{calc}) orientations, we simply chose to compare experiment and theory by fixing the tilt angle (τ) and scanning through ϕ_{calc} within the bound regions of Fig. 4. By sweeping a white rectangle in Fig. 4 through the
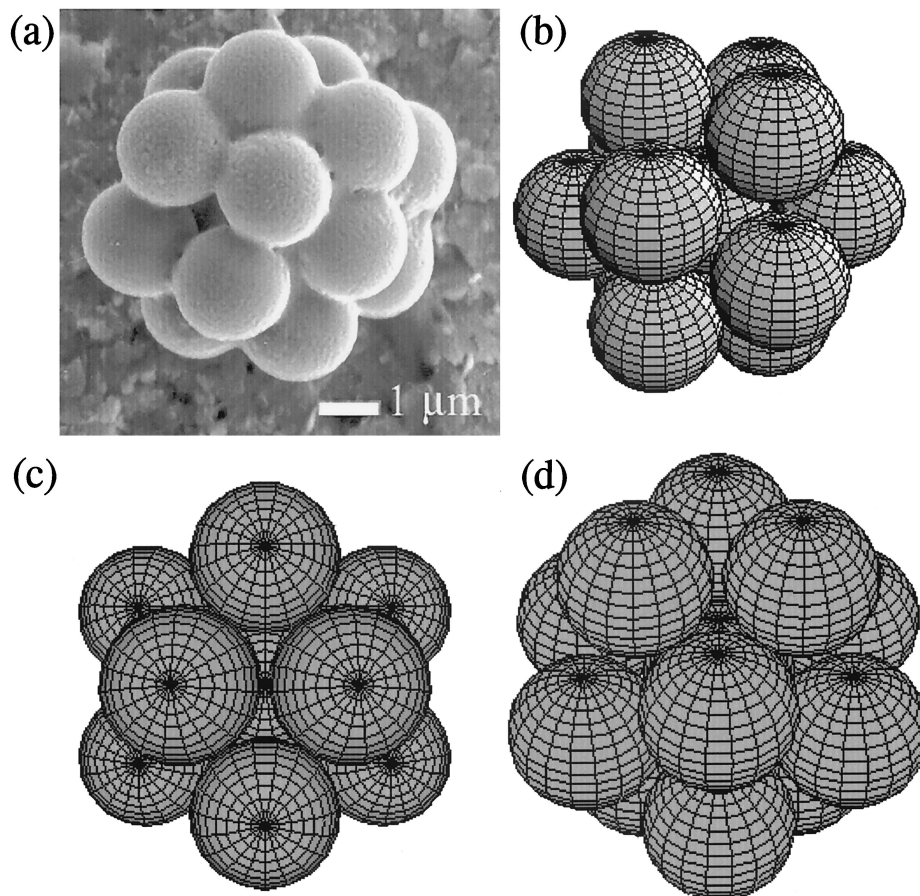
Fig. 3. (a) SEM image of a typical cluster for which TAOS measurements were performed. (b) Mathematica default representation of the cluster used in the numerical calculations. The primary particle coordinates are given in Table 1. (c) Representation of the unrotated ($\tau = 0°$) theoretical cluster viewed along the z axis of the calculation frame, i.e., the cluster as seen from the incident plane wave. (d) Realization of the theoretical cluster rotated by 45° and viewed along the z axis of the calculation frame.

bound region, we could choose a portion of the calculated TAOS pattern to compare with the experimental results. Comparisons are made at various values of ϕ_{calc} until reasonable correspondence is found. This method for comparing our results is supported by calculations of light scattering by the theoretical cluster (Fig. 3) for parallel and perpendicular polarizations. These calculations, which are equivalent to keeping the polarization fixed and rotating the cluster through 90°, show little difference in the TAOS pattern and thus give us the confidence that our comparison method is reasonable.

Figure 5 shows eight representative TAOS measurements made in the near-forward region ($16° \leq \phi_{lab} \leq 44°$, $87° \leq \theta_{lab} \leq 94°$). They demonstrate the rich speckle pattern that arises from near-field interactions and multiple-scattering events among the primary particles. Figure 6 shows eight calculated TAOS patterns that qualitatively resemble the experimental data of Fig. 5. These eight plots are representations of different ϕ_{calc} locations of the data within the bound regions of Fig. 4 ($16° \leq \theta_{calc} \leq 44°$) presented in a format such that the angular coverage within each plot corresponds to the same area as that for the ICCD camera. The best correspondence is found for the cluster tilted by 45° and is the result of the lack of symmetry for this cluster orientation. For the untilted cluster a large amount of symmetry exists because the primary particles are arranged in an almost crystalline fashion. Tilting the cluster by 5° does little to remove the symmetry of the aggre-

Table 1. Coordinates of the Spheres Used for the Cluster Calculation

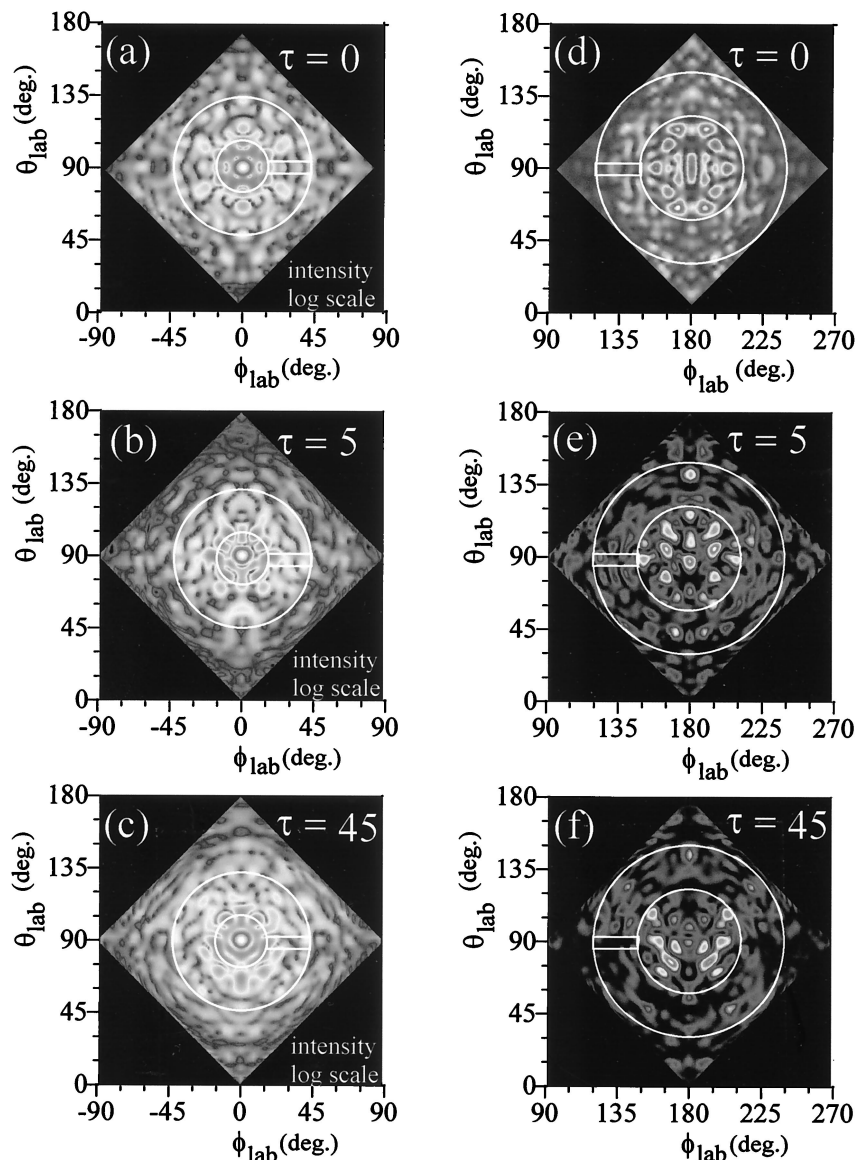| Sphere Number	x	y	z
1	0.000	0.000	0.000
2	1.925	−1.189	0.000
3	0.000	1.925	−1.189
4	−1.189	0.000	1.925
5	0.000	−1.925	−1.189
6	1.189	0.000	1.925
7	−1.925	1.189	0.000
8	1.189	0.000	−1.925
9	−1.925	−1.189	0.000
10	1.925	1.189	0.000
11	0.000	−1.925	1.189
12	−1.189	0.000	−1.925
13	0.000	1.925	1.189

Fig. 4. Forward and backward TAOS calculations transformed into the laboratory coordinates for three cluster orientations: 0°, top; 5°, middle; 45° bottom.

gate; however, some correspondence with the experiment is found.

For the near-backward region ($120° \leq \phi_{lab} \leq 148°$, $87° \leq \theta_{lab} \leq 94°$), eight representative TAOS measurements are shown in Fig. 7. They too show the rich speckle pattern; however, the intensity patches seem to exhibit a more random orientation. The same type of comparison between experiment and calculation is presented for the backward-scattering case. Figure 8 shows the results of this comparison, with eight numerical calculations for the TAOS patterns in the bound angular region of Fig. 4 ($120° \leq \theta_{calc} \leq 148°$). A greater correspondence between experiment and theory is found for the cluster tilted by 45°; however, in spite of the high symmetry, correspondence is also seen for the untilted and the 5° tilted cluster orientations.

Although the comparisons presented in Figs. 5 and 6 and in Figs. 7 and 8 are not quantitative, they do show some common features that persist in both the experimental and theoretical results. Most notably, the comparison shows a correspondence in the frequency of the speckle features as well as relatively good agreement in the size of the peaks. Previously reported TAOS measurements of larger (≈ 11-μm) clusters of the 2.29-μm-diameter psl spheres demonstrate a higher-frequency speckle pattern with a corresponding decrease in the peak size.[3] Quantitative comparisons between experiment and theory are not possible because of the limited information regarding cluster configuration and orientation that was available at the time of the measurement. Despite our inability to make a quantitative comparison, there are some features present in all the calculations that
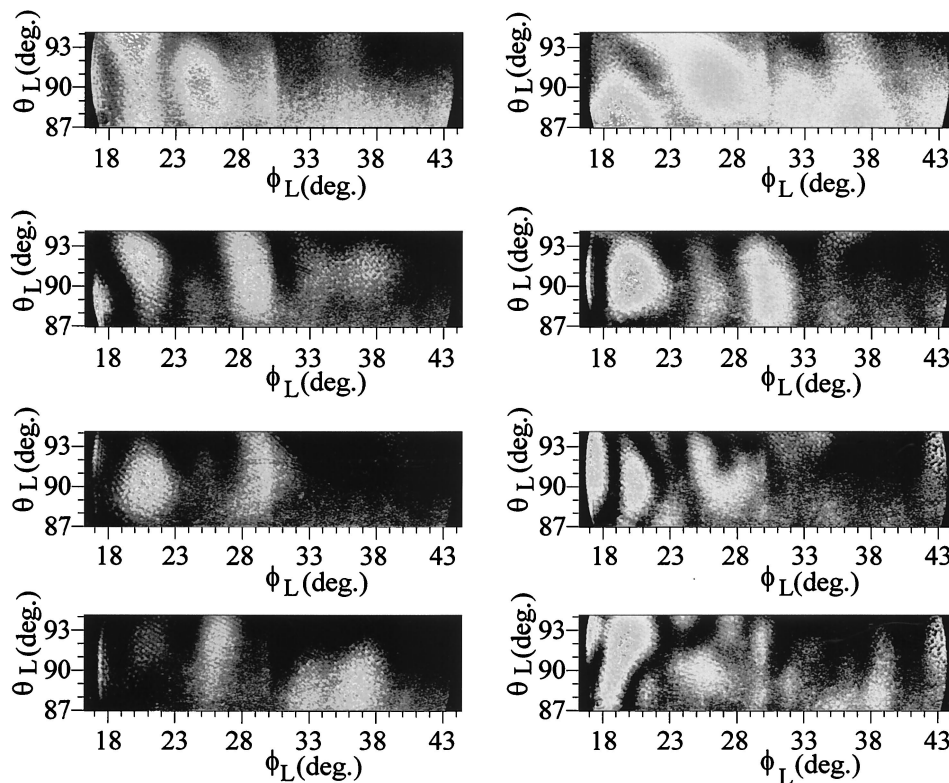
Fig. 5. Eight representative TAOS measurements in the near-forward scattering direction.

are observed in the experiment. It is these features that should make it possible to determine the primary particle size as well as the overall cluster size. What is needed to better predict the TAOS is knowledge of the cluster orientation and a more-detailed understanding of the nature of aggregate formation to permit the primary particles of the cluster used in the calculations to be more realistically positioned. The presence of internal irregularities, e.g., unevaporated liquid within the crystal, can also have a dramatic effect on the TAOS.[7]

What we have presented is merely one case demonstrating qualitative agreement among the features found in the experimentally observed and numerically calculated TAOS patterns for an aggregate of spheres. What then happens if the size of the primary particle is changed? The effect of the primary particles on the overall scattering pattern is quite dramatic. The close proximity of the spheres and the corresponding surface roughness of the aggregate lead to near-field effects and multiple-scattering events that further lead to the breakdown of the smooth, continuous contours associated with scattering from a single sphere. Although we can infer based on our knowledge of light scattering from a sphere and previous experiments on clusters[3] that, as the aggregate size changes, the speckle pattern becomes more or less dense, the effect of size changes in the primary particles is less obvious. One might expect that as the primary particle became smaller the islands of intensity would become broader. In fact, such appears to be the case. Figure 9 shows TAOS

pattern calculations of the forward-scattering region in the laboratory frame for two unrotated ($\tau = 0°$) clusters that have the same size but contain different-sized primary particles. The effect of primary particle size is noticeable in the forward scattering, where diffraction is the dominant component of the scattering. In Fig. 9(a) the cluster contains 2-μm-diameter spheres, whereas the cluster in Fig. 9(b) comprises 2.29-μm-diameter spheres. Even for this modest change in diameter one can clearly see the effect that primary particles have on the angular intensity distribution. The structure of both clusters is the same as that shown in Fig. 3(c). This symmetry is clearly seen in the diffraction regime of the forward-scattered light. The intensity patches in the TAOS pattern of Fig. 9(a) are broader, and there appear to be fewer of them. In contrast, the TAOS pattern in Fig. 9(b) shows sharper peaks, particularly in the diffraction-dominated region, as well as a higher speckle density elsewhere. The TAOS patterns in Fig. 9 are simply meant to corroborate our results presented above, and a more-detailed study of the nature of light scattering from clusters that contain different-sized primary particles will be presented at a later date.[27]

5. Summary

Although the results presented are not yet quantitative, they do offer insight into the nature of light scattering by an aggregate of spherical primary particles. The correspondence between the experimentally observed two-dimensional angular optical
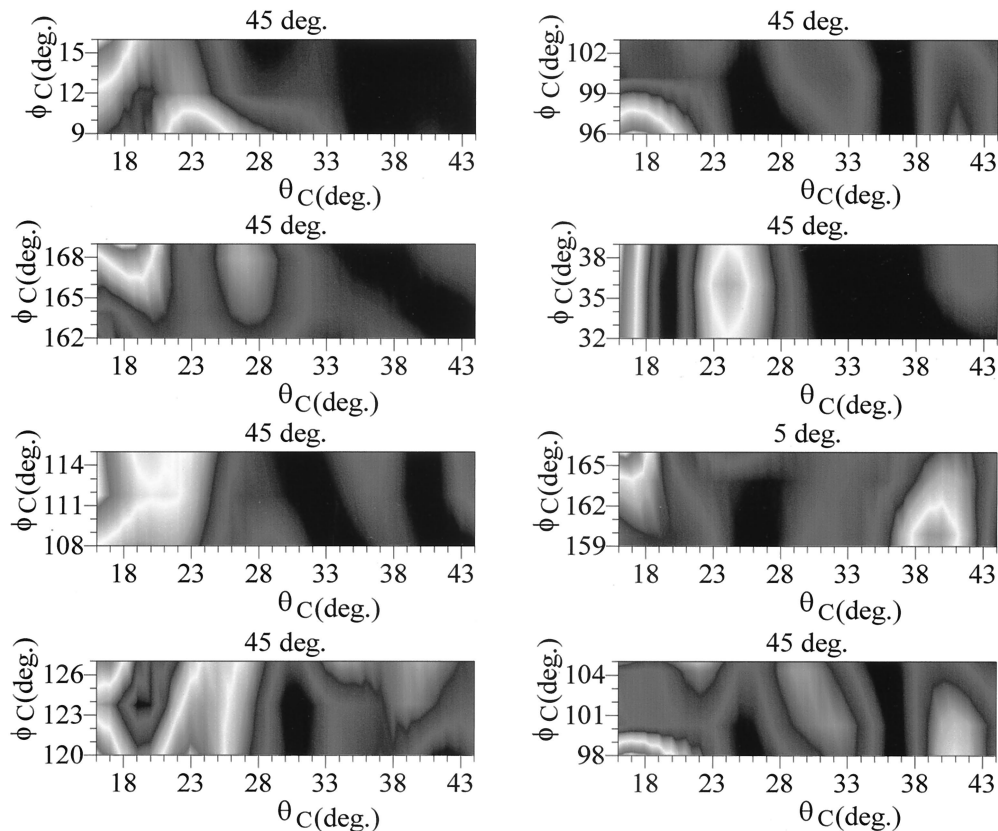
Fig. 6. Near-forward TAOS calculations, showing qualitative features found in the experiments.

scattering and the numerically calculated patterns is good. Both experiment and theory yield the same qualitative features within the same-sized angular region. The difficulty in making quantitative comparisons lies in unraveling the means by which aggregates of spheres are formed and determining a means for discerning the orientation of the falling cluster at the moment of the TAOS measurement. Furthermore, providing for larger angular coverage with the detector would improve the ability to make quantitative comparisons. By far the easiest of these improvements lies in the large-format detector capable of recording the TAOS patterns over a wide angular range.

The complicated morphology of airborne microparticle aggregates makes understanding their light-scattering properties a challenging task. From an experimental viewpoint it is almost impossible to know the exact structure, orientation, and number of primary particles of the cluster under study. Likewise, memory limits and time constraints often restrict the sizes of aggregates that can be studied computationally, and the cluster structure is somewhat artificial and crystalline. Despite these difficulties, experiments and theory are rapidly finding a common ground, and computational techniques, computer speed with larger memory, and a large format CCD camera will improve in the future.

Appendix A

1. Translation Addition Theorem

Stein[28] and Cruzan[29] introduced the translation addition theorem of spherical wave functions. This theorem is formed by three different kinds of relation:

$$
\begin{aligned}
\Re e\, \Psi_{1mn}(kr_i, \theta_i, \phi_i) = \sum_{\mu\nu} \Re e\, A_{\mu\nu}^{mn}(r_{ij}, \theta_{ij}, \phi_{ij}) \\
\times \Re e\, \Psi_{1\mu\nu}(kr_j, \theta_j, \phi_j) \\
+ \Re e B_{\mu\nu}^{mn}(r_{ij}, \theta_{ij}, \phi_{ij}) \\
\times \Re e\, \Psi_{2\mu\nu}(kr_j, \theta_j, \phi_j),
\end{aligned}
$$

$$
\begin{aligned}
\Re e\, \Psi_{2mn}(kr_i, \theta_i, \phi_i) = \sum_{\mu\nu} \Re e B_{\mu\nu}^{mn}(r_{ij}, \theta_{ij}, \phi_{ij}) \\
\times \Re e\, \Psi_{2\mu\nu}(kr_j, \theta_j, \phi_j) \\
+ \Re e\, A_{\mu\nu}^{mn}(r_{ij}, \theta_{ij}, \phi_{ij}) \\
\times \Re e\, \Psi_{2\mu\nu}(kr_j, \theta_j, \phi_j). \quad (A1)
\end{aligned}
$$

If $r < r_0$,

$$
\begin{aligned}
\Psi_{1mn}(kr_i, \theta_i, \phi_i) = \sum_{\mu\nu} A_{\mu\nu}^{mn}(r_{ij}, \theta_{ij}, \phi_{ij}) \\
\times \Re e\, \Psi_{1\mu\nu}(kr_j, \theta_j, \phi_j) \\
+ B_{\mu\nu}^{mn}(r_{ij}, \theta_{ij}, \phi_{ij}) \\
\times \Re e\, \Psi_{2\mu\nu}(kr_j, \theta_j, \phi_j),
\end{aligned}
$$
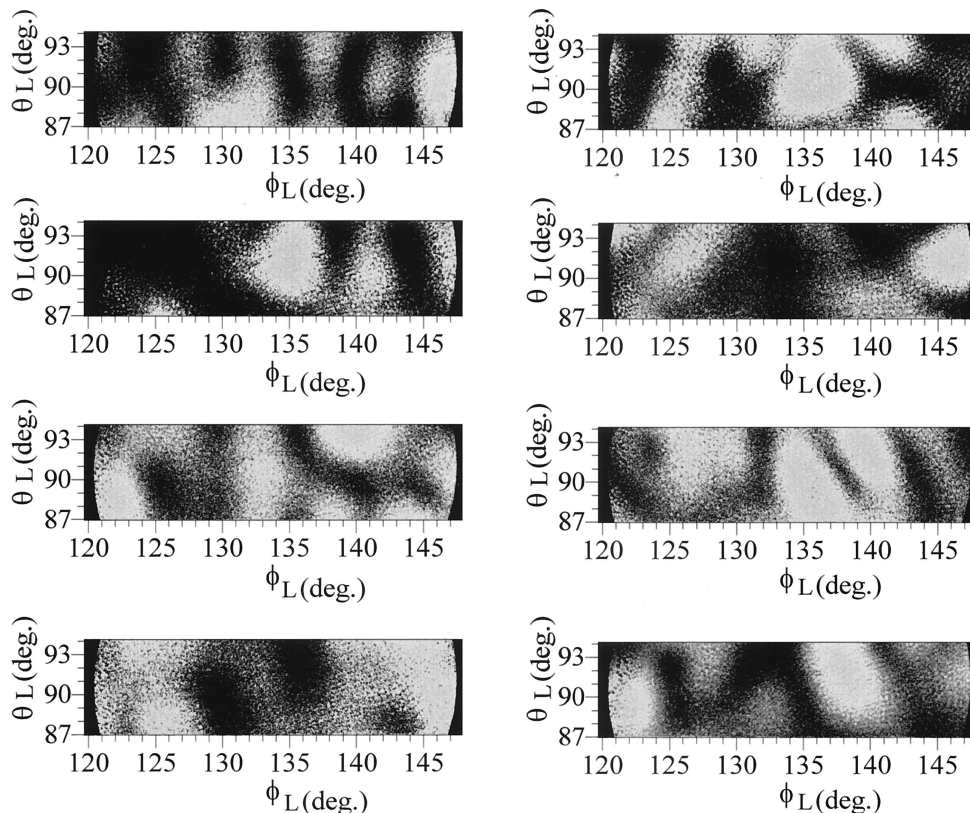
Fig. 7. Eight representative TAOS measurements in the near-backward scattering direction.

$$\Psi_{2mn}(kr_i, \theta_i, \phi_i) = \sum_{\mu\nu} B_{\mu\nu}^{mn}(r_{ij}, \theta_{ij}, \phi_{ij})$$
$$\times \Re e \; \Psi_{1\mu\nu}(kr_j, \theta_j, \phi_j)$$
$$+ A_{\mu\nu}^{mn}(r_{ij}, \theta_{ij}, \phi_{ij})$$
$$\times \Re e \; \Psi_{2\mu\nu}(kr_j, \theta_j, \phi_j). \quad \text{(A2)}$$

If $r > r_0$,

$$\Psi_{1mn}(kr_i, \theta_i, \phi_i) = \sum_{\mu\nu} \Re e \, A_{\mu\nu}^{mn}(r_{ij}, \theta_{ij}, \phi_{ij})$$
$$\times \Psi_{1\mu\nu}(kr_j, \theta_j, \phi_j)$$
$$+ \Re e \, B_{\mu\nu}^{mn}(r_{ij}, \theta_{ij}, \phi_{ij})$$
$$\times \Psi_{2\mu\nu}(kr_j, \theta_j, \phi_j),$$

$$\Psi_{2mn}(kr_i, \theta_i, \phi_i) = \sum_{\mu\nu} \Re e \, B_{\mu\nu}^{mn}(r_{ij}, \theta_{ij}, \phi_{ij})$$
$$\times \Psi_{1\mu\nu}(kr_j, \theta_j, \phi_j)$$
$$+ \Re e \, A_{\mu\nu}(r_{ij}, \theta_{ij}, \phi_{ij})$$
$$\times \Psi_{2\mu\nu}(kr_j, \theta_j, \phi_j). \quad \text{(A3)}$$

$A_{\mu\nu}^{mn}$, $\Re e \, A_{\mu\nu}^{mn}$, $\beta_{\mu\nu}^{mn}$, and $\Re e B_{\mu\nu}^{mn}$ are translation coefficients that can be expressed in terms of Gaunt coefficients:

$$A_{\mu\nu}^{mn} = \frac{\sqrt{\gamma_{mn}}}{\sqrt{\gamma_{\mu\nu}}} (-1)\mu \sum_p a(m, n|-\mu, \nu|p)a(n, \nu, p)$$
$$\times h_p(ka)P_p^{m-\mu}(\cos \theta_{0k})\exp[i(m - \mu)\phi_{0k}], \quad \text{(A4)}$$

$$B_{\mu\nu}^{mn} = \frac{\sqrt{\gamma_{mn}}}{\sqrt{\gamma_{\mu\nu}}} (-1)^{\mu+1} \sum_p a(m, n|-\mu, \nu|p, p$$
$$- 1)b(n, \nu, p)h_p(ka) P_p^{m-\mu}(\cos \theta_{0k})$$
$$\times \exp[i(m - \mu)\phi_{0k}]. \quad \text{(A5)}$$

The Gaunt coefficients $a(m, n| - \mu, \nu|p)$ and $a(m, n| - \mu, \nu|p, p - 1)$ are expressed in terms of Wigner 3-j symbols

$$\begin{bmatrix} j_1 & j_2 & j_3 \\ 0 & 0 & 0 \end{bmatrix},$$

which are related to Clebsch–Gordon coefficients:

$$a(m, n|\mu, \nu|p) = (-1)^{m+\mu}(2p + 1)$$
$$\times \left[\frac{(n + m)!(\nu + \mu)!(p - m - \mu)!}{(n - m)!(\nu - \mu)!(p + m + \mu)!} \right]^{1/2}$$
$$\times \begin{bmatrix} n & \nu & p \\ 0 & 0 & 0 \end{bmatrix} \begin{bmatrix} n & \nu & p \\ m & \mu & -m - \mu \end{bmatrix}, \quad \text{(A6)}$$

$$a(m, n|\mu, \nu|p, q) = (-1)^{m+\mu}(2p + 1)$$
$$\times \left[\frac{(n + m)!(\nu + \mu)!(p - m - \mu)!}{(n - m)!(\nu - \mu)!(p + m + \mu)!} \right]^{1/2}$$
$$\times \begin{bmatrix} n & \nu & q \\ 0 & 0 & 0 \end{bmatrix} \begin{bmatrix} n & \nu & p \\ m & \mu & -m - \mu \end{bmatrix}. \quad \text{(A7)}$$
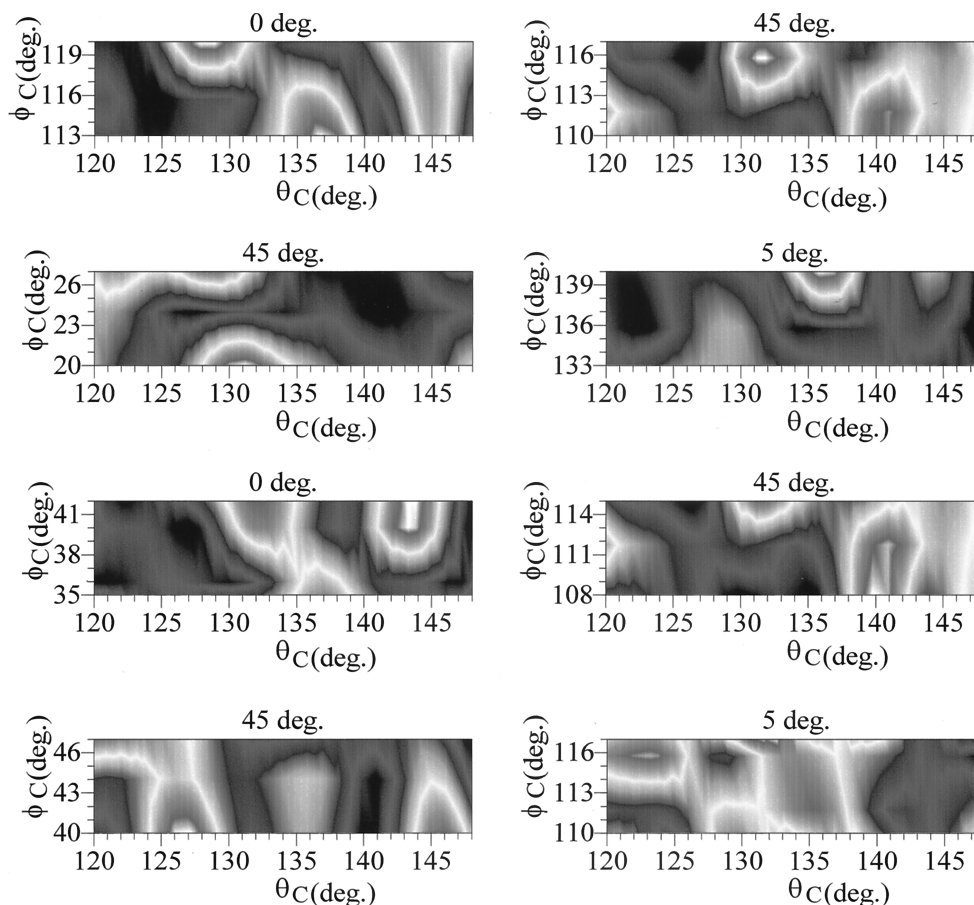
Fig. 8.   Near-backward TAOS calculations, showing qualitative features found in the experiments.

Evaluation of the translation coefficients by use of Stein's formalism leads to a summation on a parameter p by use of Eqs. (A4) and (A5). It seems that, since the paper of Peterson and Ström, there is some confusion in the literature about the correct values that p takes. Xu has partially explicated the problem.[23]   Our study leads to the following explanation: In accordance with the rules of addition of the kinetic moment, parameter p should assume all the integer values $p = n \oplus v = (n + v), (n + v - 1), (n + v - 2), \ldots, |n - v|$. However, Wigner 3-$j$ symbols vanish if $j_1 + j_2 + j_3$ is an odd integer. Then the contribution of the p summation to the $A_{\mu\nu}^{mn}$ coefficient value is null when, because of the Wigner 3-j symbol

$$\begin{bmatrix} n & v & p \\ 0 & 0 & 0 \end{bmatrix},$$

p takes the values $(n + v - 1), (n + v - 3)$ until $|n - v| + 1$. In the case of the $B_{\mu\nu}^{mn}$ coefficient, the Wigner 3-j symbol is

$$\begin{bmatrix} n & v & q \\ 0 & 0 & 0 \end{bmatrix}$$

where $q = p - 1$. Then the contribution of the p summation is null when p takes on the following values: $(n + v), (n + v - 2)$ until $|n - v|$. That is, in the evaluation of the $A_{\mu\nu}^{mn}$ coefficients, p takes on

the values from $|n - v|$ to $(n + v)$ in steps of 2; and in the evaluation of the $B_{\mu\nu}^{mn}$ coefficients, p takes on the values from $|n - v| + 1$ to $(n + v)$ in steps of 2.

Index n is linked to the multipole expansion representative of each dielectric sphere of the cluster. The computation of the T matrix through the extended boundary condition technique requires the truncation of an infinite-dimensional integral matrix equation to a value $n = n_{\max}$. This value must be large enough to represent the physically relevant partial waves correctly but not too large to be useful numerically. It is usually admitted that Wiscombe's criterion allows for an accurate determination of this value.[31]   There are as many different $n_{\max}$ as the number of different types and sizes of sphere. We truncate the incident and all the series expansions of the scattered fields at the larger $n_{\max}$ value. Then f and a are column vectors of dimension $n_{\max} \times 1$.

2.   Truncation of the Translation Addition Theorem Series

The computation of the N-spheres problem assumes that the series expansions of the translation addition theorem [Eqs. (A1), (A2), and (A3)] are uniformly convergent. Therefore we can truncate them at $v = v_{\max}$, assuming that the resultant error is small enough if $v_{\max}$ is sufficiently large.

The $\bar{\alpha}(i, j)$ matrices describe the continuity of the tangential components of all the scattered electric
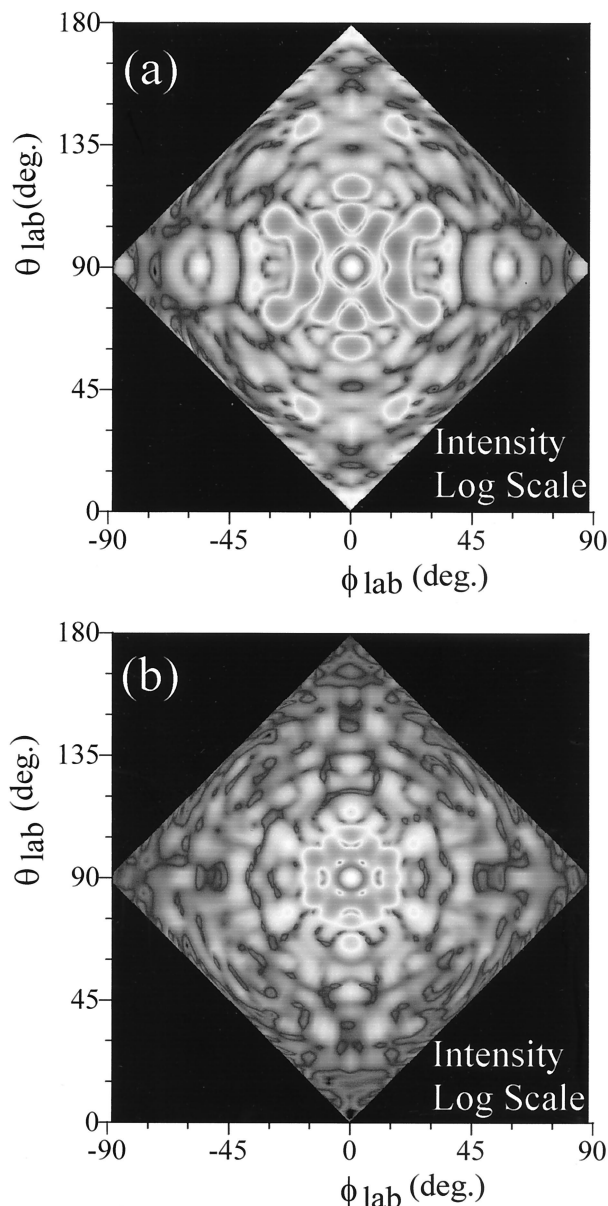
Fig. 9. Forward TAOS calculations for two clusters of the same size that comprise primary particles with different sizes: (a) cluster containing 2.0-μm-diameter spheres, (b) cluster containing 2.26-μm-diameter spheres.

fields across each surface of the ith sphere. Then, in an iterative formalism, $\nu_{\max}$ represents the approximation's order of multiple-scattering effects in the system. Its maximal value for convergence is approximately equal to $n_{\max}$. In the recursive algorithm, all multiple-scattering effects are taken into account during the matrix inversion of Eq. (2.21). Following the analytical coherence of the RTMA formalism, $\nu_{\max} = n_{\max}$. Therefore the $\bar{\alpha}(i, j)$ matrices' dimensions are $[2n_{\max}(n_{\max} + 2)]^2$.

Equation (2.17) can also be described as a phase shift of the incident plane wave when it travels from origins O_0 to O_i:

$$\mathbf{a}^i = \mathbf{a}^0 \exp(ik_{\mathrm{inc}}r_i). \tag{A8}$$

Starting with $\nu_{\max} = n_{\max}$, we calculate the absolute variation between the numerical results of Eqs. (A8) and (2.17) for each vector's component owing to the variation of $\nu_{\max}$. The convergence speed also depends on the distance and the orientation between the coordinate systems. Nevertheless, at $\nu_{\max} = n_{\max}$ the maximal absolute variation is approximately 1. When $\nu_{\max} = 2n_{\max}$, the variation is only 6–10, and it is not until $\nu_{\max} = 3n_{\max}$ that an absolute variation of 10–15 occurs in the best cases. The dimensions of the $\bar{\beta}(i, 0)$ matrices are $4n_{\max}(n_{\max} + 2) \times \nu_{\max}(\nu_{\max} + 2)$.

Because of the analytical coherence of the RTMA formalism,[24] the series [Eqs. (A3)] has to be truncated at the same order $\nu_{\max}$ as Eqs. (A2). The dimension of the matrices $\bar{\beta}(0, i)$ is $4\nu_{\max}(\nu_{\max} + 2) \times n_{\max}(n_{\max} + 2)$. The limits of convergence that we have encountered for the $\bar{\beta}(i, 0)$ matrices are still present and are propagated into numerical evaluations.

We can see that, if the indices $n_{\max}$ and $\nu_{\max}$ become too large, the numerical evaluations of the matrices $\bar{\alpha}(i, j)$, $\bar{\beta}(i, 0)$, and $\bar{\beta}(0, i)$ are limited by the free memory available on the computer, realistic computing time, and numerical convergence of the series. With these three factors taken into account, the computation of the total scattered field by a random cluster in terms of a single expansion on one principal coordinate system is impracticable most of the time. Consequently, the scattering parameter of the sphere cluster (cross sections and scattering matrix) cannot be evaluated.

To circumvent this difficulty, Borghese et al.,[32] Mackowski and Mishchenko,[5] and Fuller[4] derived explicit expressions for the total cross sections (scattering, extinction, and absorption) of the sphere cluster without any need for a single representation of the total scattered field. This formalism is called the sphere-centered formulation. Moreover, Xu[23] recently introduced a formalism with which to obtain a single expression of the total scattered field in the far-field region. This approach is the most suitable for obtaining differential scattering cross sections of an aggregate without taking the convergence of the translation addition theorem series [Eqs. (A3)] into account. Indeed, for an arbitrary point M in the far-field region at vector positions $\mathbf{r}$ in the principal system and $\mathbf{r}_i$ in the coordinate system of the ith sphere, one can consider that these two vectors are parallel. By introducing Δ_i as the path variation that is due to the relative position between the principal and the ith systems, we obtain $r_i = r - \Delta_i$, with $\Delta_i = \hat{e}_r \cdot \mathbf{r}_{0i}$, where $\hat{e}_r$ is a unit vector pointed in the direction of M. Then it can be shown that, in the far-field region, the translation coefficient can be written as

$$\Re A_{\mu\nu}^{mn}(kr_{0i}, \theta_{0i}, \phi_{0i}) = \delta_{n\nu}\delta_{\mu m}\exp(-ik\Delta_i),$$
$$\Re B_{\mu\nu}^{mn}(kr_{0i}, \theta_{0i}, \phi_{0i}) = 0. \tag{A9}$$

This formulation leads to a simplification of the analytical formulation of $\bar{\beta}(0, i)$. Finally, the total field

scattered by the entire cluster of Eq. (2.18) can be written in the far-field region as

$$\mathbf{f}^{T(N)} = \sum_{i=1}^{N} \exp(-ik\Delta_i)\mathbf{f}^{i(N)}. \qquad (A10)$$

3. Recursive T-Matrix Formulation in the Far-Field Region

Because of the problems introduced in the Subsections A.1 and A.2, we introduce a new model of multiple scattering computation by an aggregate of spheres based on the RTMA algorithm developed by Chew[24] modified to bypass the convergence problem of Eqs. (A.1). Indeed, the evaluation of the incident field on each sphere is made by use of a phase-shift formalism instead of a matrix calculation. Then, in the second stage, to circumvent the convergence problem of Eqs. (A3), we use the far-field approximation introduced by Xu.[23] The fundamental equations of this model are

$$\bar{\mathbf{T}}^{N+1(N+1)} = \left[\bar{\mathbf{I}} - \bar{\mathbf{T}}^{N+1(1)} \sum_{i=1}^{n} \bar{\alpha}(N+1, i)\bar{\mathbf{T}}^{i(N)}\bar{\alpha}(i, N+1) \right]^{-1} \bar{\mathbf{T}}^{N+1(1)} \left\{ \bar{\mathbf{I}} + \sum_{i=1}^{n} \bar{\alpha}(N+1, i)\bar{\mathbf{T}}^{i(N)} \exp[i\mathbf{k}_{\text{inc}}(\mathbf{r}_{N+1} - \mathbf{r}_i)] \right\}, \qquad (A11)$$

$$\bar{\mathbf{T}}^{i(N+1)} = \bar{\mathbf{T}}^{i(N)}\{\bar{\mathbf{I}} + \bar{\alpha}(i, N+1)\bar{\mathbf{T}}^{N+1(N+1)} \times \exp[i\mathbf{k}_{\text{inc}}(\mathbf{r}_{N+1} - \mathbf{r}_i)]\}, \qquad i \leq N, \qquad (12)$$

$$\mathbf{f}^{(N+1)} = \sum_{i=1}^{N+1} \mathbf{f}^{i(N+1)} \exp(-ik\Delta_i), \qquad (A13)$$

$$\mathbf{f}^{i(N+1)} = \bar{\mathbf{T}}^{i(N+1)}\mathbf{a}^0 \exp(i\mathbf{k}_{\text{inc}}\mathbf{r}_i). \qquad (A14)$$

References and Notes

1. R. H. Zerull, B. Å S. Gustafson, K. Schulz, and E. Thiele-Corbach, "Scattering by aggregates with and without an absorbing mantle: microwave analog experiments," Appl. Opt. **32,** 4088–4100 (1993).
2. G. Videen, D. Ngo, and M. B. Hart, "Light scattering from a pair of conducting, osculating spheres," Opt. Commun. **125,** 275–287 (1996).
3. S. Holler, Y.-L. Pan, R. K. Chang, J. R. Bottiger, S. C. Hill, and D. B. Hillis, "Two-dimensional angular optical scattering for the characterization of airborne microparticles," Opt. Lett. **23,** 1489–1491 (1998).
4. K. A. Fuller, "Scattering and absorption cross sections of compounded spheres. I. Theory for external aggregation," J. Opt. Soc. Am. A **11,** 3251–3260 (1994).
5. D. W. Mackowski and M. I. Mishchenko, "Calculation of the T matrix and the scattering matrix for ensembles of spheres," J. Opt. Soc. Am. A **13,** 2266–2278 (1996).
6. D. Ngo, G. Videen, and R. Dalling, "Chaotic light scattering from a system of osculating, conducting spheres," Phys. Lett. A **227,** 197–202 (1997).
7. G. Videen, W. Sun, and Q. Fu, "Light scattering from irregular tetrahedral aggregates," Opt. Commun. **156,** 5–9 (1998).
8. D. R. Bowes, A. M. Langer, and A. N. Rohl, "Nature and range of mineral dusts in the environment," Philos. Trans. R. Soc. London Ser. A **286,** 593–610 (1977).
9. E. Frejafon, J. Kasparian, P. Rambaldi, B. Vezin, V. Boutou, J. Yu, M. Ulbricht, D. Weidauer, B. Ottobrini, E. de Saeger, B. Krämer, T. Leisner, P. Rairoux, L. Wöste, and J. P. Wolf, "Laser applications for atmospheric pollution monitoring," Eur. J. Phys. D **4,** 231–238 (1998).
10. J. E. Hansen and L. D. Travis, "Light scattering in planetary atmospheres," Space Sci. Rev. **16,** 527–610 (1974).
11. D. R. Huffman, "Interstellar grains. The interaction of light with a small particle system," Adv. Phys. **26,** 129–230 (1977).
12. C. M. Sorensen, J. Cai, and N. Lu, "Light scattering measurements of monomer size, monomers per aggregate and fractal dimension for soot aggregates in flames," Appl. Opt. **31,** 6547–6557 (1992).
13. R. G. Pinnick, S. C. Hill, P. Nachman, G. Videen, G. Chen, and R. K. Chang, "Aesosol fluorescence spectrum analyzer for measurement of single micronsized airborne biological particles," Aerosol Sci. Technol. **28,** 95–104 (1998).
14. P. L. Marston and E. H. Trinh, "Hyperbolic umbilic diffraction catastrophe and rainbow scattering from spheroidal drops," Science **312,** 529–531 (1984).
15. P. L. Marston, "Cusp diffraction catastrophe from spheroids: generalized rainbows and inverse scattering," Opt. Lett. **10,** 588–590 (1985).
16. J. P. Barton, "Light scattering calculations for irregularly shaped axisymmetric particles of homogeneous and layered compositions," Meas. Sci. Technol. **9,** 151–160 (1998).
17. J. P. Barton, "Electromagnetic field calculations for a sphere illuminated by a higher-order Gaussian beam. II. Far-field scattering," Appl. Opt. **37,** 3339–3344 (1998).
18. G. Mie, "Beitrage zur optik trüber medien speziell kolloidaler metallösungen," Ann. Phys. (Leipzig) **25,** 377–445 (1908).
19. J. Stratton, *Electromagnetic Theory* (McGraw-Hill, New York, 1941).
20. C. F. Bohren and D. R. Huffman, *Absorption and Scattering of Light by Small Particles* (Wiley, New York, 1983).
21. P. C. Waterman, "Symmetry, unitary, and geometry in electromagnetic scattering," Phys. Rev. D **3,** 825–839 (1970).
22. A.-K. Hamid, "Electromagnetic scattering by an arbitrary configuration of dielectric spheres," Can. J. Phys. **68,** 1419–1428 (1990).
23. Y.-L. Xu, "Electromagnetic scattering by an aggregate of spheres: far field," Appl. Opt. **36,** 9496–9508 (1997).
24. W. C. Chew, *Waves and Field in Inhomogeneous Media*, IEEE Press Series on Electromagnetic Waves (Institute of Electrical and Electronics Engineers, Piscataway, N.J., 1990).
25. J. R. Bottiger, P. J. Deluca, E. W. Stuebing, and D. R. VanReenen, "An ink jet aerosol generator," J. Aerosol Sci. **29,** Suppl. 1, 965–966 (1998).
26. M. Born and E. Wolf, *Principles of Optics*, 6th ed. (Pergamon, Oxford, 1980).
27. J.-C. Auger, Laboratoire d'Optiques des Solides, Unité Mixte de Recherche 7601, Université Pierre et Maríe Curie, Paris,

France, and G. Videen, are preparing a manuscript to be called "Spatial light scattering and sphere clusters."

28. S. Stein, "Addition theorems for spherical wave function," Q. Appl. Math. **19,** 15–24 (1961).

29. O. R. Cruzan, "Translation addition theorems for spherical vector wave functions," Q. Appl. Math. **20,** 33–40 (1962).

30. B. Peterson and S. Ström, "T matrix for electromagnetic scattering from an arbitrary number of scatterers and representation of $E(3)$," Phys. Rev. D **8,** 3661–3677 (1973).

31. W. J. Wiscombe, "Improve Mie scattering algorithms," Appl. Opt. **19,** 1505–1509 (1980).

32. F. Borghese, P. Denti, R. Saija, G. Toscano, and O. I. Sindoni, "Multiple electromagnetic scattering from a cluster of spheres. I. Theory," Aerosol Sci. Technol. **3,** 227–235 (1984).